 VoR: https://doi.org/10.1016/j.still.2013.12.008

Assessment of water and air permeability of chernozem supported by image analysis

Maja Bryk, Beata Kołodziej
Institute of Soil Science, Environment Engineering and Management, University of Life Sciences in Lublin, Leszczyńskiego 7, 20-069 Lublin, Poland

Corresponding author: Maja Bryk
Institute of Soil Science, Environment Engineering and Management
Leszczyńskiego 7, 20-069 Lublin, Poland
maja.bryk@up.lublin.pl, majabryk@post.pl, phone +48 81 5248148

Abstract

We aimed at the assessment of water and air permeability of a Haplic Chernozem developed from loess. The laboratory permeability measurements were presented against a number of morphometric indices that characterize the pore system in this soil, and were obtained by computer-aided image analysis on the basis of large resin-impregnated soil opaque blocks. Two indices of soil pore connectivity are proposed, i.e. the index of soil pore network growth rate and the percolation number. Basic soil properties were evaluated (soil texture, TOC, carbonates, pH, particle and soil bulk density, total porosity). The saturated hydraulic conductivity, and soil water content, air capacity and permeability at –15.54 kPa and –9.81 kPa were measured. From the samples with preserved structure, resin-impregnated soil opaque blocks 8×9 cm in size were prepared and then used for morphological and morphometric structure analysis. The preliminary image analysis was made to find the best representation of the actual chernozem pore system. The images were modified by applying the morphological closing with or without the spike noise, which modelled tiny pores missed during scanning. Consequently, the macroporosity of the images approximated the air capacity at potentials –15.54 and –9.81 kPa. During the extended image analysis, we calculated: the index of soil pore network growth rate; the percolation number; the average cross-sectional size of the pore; the total length of pore path; the relative volume of pores overlapping the left and right, and the top and bottom image edge; the relative volume of pores connecting the left and right and the top and bottom edge of the image. The correlation coefficients between the parameters' values obtained from image analysis and from laboratory permeability measurements were calculated.

The water and air permeability and the air capacity of the chernozem decreased with depth

into the soil pedon. With decrease in the saturated hydraulic conductivity, measured in the laboratory, there was a decrease in the relative volumes of pores overlapping the left and right and upper and lower edges of the image, obtained from image analysis. The air permeability was positively correlated with the index of pore network growth rate. Morphological and morphometric image analysis confirmed that the most important parameters determining the transport of fluids in the soil are continuity of the pore system and pore volume. Based on the results obtained from image analysis one can formulate qualitative conclusions concerning the water and air permeability of soil.

Keywords
soil structure, image analysis, pore connectivity indices, pore simulation, air permeability, hydraulic conductivity

1. Introduction

Determining the water and air permeability of soil enables to quantitatively characterize the ability of the soil to transport substances (Słowińska-Jurkiewicz et al., 2001). The rate of movement of solutions in the soil affects the availability of the dissolved nutrients to the organisms living in the soil, while aeration of the soil is related to the air capacity and permeability, and determines the oxygenation of the soil, as well as the soil ability to transport gases. For this reason, water and air permeability of the soil is of interest to a wide range of specialists in agricultural and environmental studies (Badorreck et al., 2013; Bryk et al., 2007; Bryk, 2009; Bryk and Kołodziej, 2009; Horn and Smucker, 2005; Kołodziej et al., 2007; Maruszewski and Dembski, 2008; Schjønning and Thomsen, 2013).

The transport of water, gases and solutes in soil is primarily determined by the soil structure and is shaped by the nature of the pores and the presence or absence of soil aggregates (Kutílek, 2004; Vogel et al., 2006). With regard to transport processes, soil may be treated as a two-phase system consisting of a solid phase and voids. In this respect, the characteristics of the geometric properties of the soil voids and/or solid phase should be expressed in numbers so as to allow the introduction of numerical structural parameters into models describing the fluid transport in the soil. Moreover, the parameterization of the soil environment provides the basis for predicting the size of water and air permeability. One of the methods to quantify the soil structure is image analysis, based on large resin-impregnated preparations – soil opaque blocks. In this manner it is possible to link the characteristics of the soil structure with its ability to transport water and air (Kutílek and Nielsen, 2007). This, in turn, enables to predict

 VoR: https://doi.org/10.1016/j.still.2013.12.008

the impact of the external conditions (e.g. climate or management) upon the ecological functions of the soil (Boizard, et al., 2013; Mangalassery et al., 2013). A combination of the results of laboratory measurements of water and air permeability and the results of morphometric analysis provides expanded insight into the level and mechanisms of transport of substances within the soil. To our knowledge, such an approach is not sufficiently covered in the current literature.

This paper aims at the assessment of water and air permeability of a Haplic Chernozem developed from loess. The laboratory permeability measurements are presented against a number of morphometric indices that characterize the pore system in the soil, and were obtained by computer-aided image analysis on the basis of large resin-impregnated soil opaque blocks. Two indices of soil pore connectivity are proposed, namely the index of soil pore network growth rate (v_G) and the percolation number (n_{per}).

Nomenclature

$A_{A(im)}$	relative area of macropores > 21.2 μm by image analysis ($cm^2 \cdot cm^{-2}$)
CHha	Haplic Chernozem
K_S	saturated hydraulic conductivity ($m \cdot d^{-1}$)
L_A	relative perimeter length of pore cross-sections ($cm \cdot cm^{-2}$)
L_P	total length of pore path (cm)
n_{per}	percolation number
$P_{A(-15.54)}$	air permeability at soil water potential –15.54 kPa (10^{-8} $m^2 \cdot Pa^{-1} \cdot s^{-1}$)
$P_{A(-9.81)}$	air permeability at soil water potential –9.81 kPa (10^{-8} $m^2 \cdot Pa^{-1} \cdot s^{-1}$)
P_O	total soil porosity ($cm^3 \cdot cm^{-3}$)
TOC	total organic carbon ($mg \cdot g^{-1}$)
v_G	index of soil pore network growth rate ($cm^3 \cdot cm^{-3}$)
$V_{V(-15.54)}$	relative volume of macropores > 18.3 μm derived from soil-water characteristic curve ($cm^3 \cdot cm^{-3}$)
$V_{V(-9.81)}$	relative volume of macropores > 29 μm derived from soil-water characteristic curve ($cm^3 \cdot cm^{-3}$)
$V_{V(hor)}$	relative volume of pores connecting left and right edge of image ($cm^3 \cdot cm^{-3}$)
$V_{V(im)}$	relative volume of macropores > 21.2 μm by image analysis ($cm^3 \cdot cm^{-3}$)
$V_{V(L+R)}$	relative volume of pores overlapping left and right edge of image ($cm^3 \cdot cm^{-3}$)
$V_{V(U+D)}$	relative volume of pores overlapping top and bottom edge of image ($cm^3 \cdot cm^{-3}$)
$V_{V(vert)}$	relative volume of pores connecting top and bottom edge of image ($cm^3 \cdot cm^{-3}$)

 VoR: https://doi.org/10.1016/j.still.2013.12.008

$W_{V(-15.54)}$	soil water content at potential –15.54 kPa ($cm^3 \cdot cm^{-3}$)
$W_{V(-9.81)}$	soil water content at potential –9.81 kPa ($cm^3 \cdot cm^{-3}$)
ε	Euler's number (connectivity number)
λ_P	average cross-sectional size of a pore (mm)
ρ	dry soil bulk density ($Mg \cdot m^{-3}$)
ρ_s	particle density ($Mg \cdot m^{-3}$)

2. Material and methods

2.1. Laboratory tests

The study was conducted on a Haplic Chernozem developed from loess, with a sequence of horizons O-A-AC-Ck, located in Marysin Kolonia (50°30'39" N, 23°56'05" E, SE Poland) in a mesophytic deciduous forest composed of oak *Quercus robur* and *Quercus petraea*, hornbeam *Carpinus betulus*, and lime *Tilia cordata*.

While making the basic soil pit, the profile of the chernozem was carefully analysed. The soil under study was characterized by similar texture throughout the whole pedon. It did not display symptoms of excessive compaction or of the presence of hard-permeable layers. The density of the soil decreased gradually with depth and with the decreasing content of biogenic pores. Taking those observations into account, in the successive genetic horizons, points for taking samples were selected, that were characteristic and representative for the whole soil pedon. The samples were collected in 2010 from 5 soil layers: 0–8 cm (CHha1; horizons O-A), 26–34 cm (CHha2, horizon A), 60–68 cm (CHha3, horizon AC), 90–98 cm (CHha4, horizons AC-Ck), and 120–128 cm (CHha5, horizon Ck).

Samples with disturbed structure were used to determine soil texture (sand 0.05–2 mm, silt 0.002–0.05 mm, and clay <0.002 mm fraction content, $g \cdot g^{-1}$, by a combination of the hydrometer and the wet-sieve methods; Polish Society of Soil Science, 2009), total organic carbon (TOC, $mg \cdot g^{-1}$, PN-ISO 14235, 2003), the amount of carbonates ($CaCO_3$, $mg \cdot g^{-1}$, PN-ISO 10693, 2002), pH (in distilled water and in 0.01 $mol \cdot dm^{-3}$ $CaCl_2$; PN-ISO 10390, 1997) and particle density (ρ_s, $Mg \cdot m^{-3}$, PN-ISO 11508, 2001).

Moreover, in 6 replicates, soil samples with preserved structure were taken vertically into metal cylinders with a volume of 100 cm^3. These were used to determine the dry soil bulk density (ρ, $Mg \cdot m^{-3}$) and soil water content at potentials –15.54 kPa and –9.81 kPa ($W_{V(-15.54)}$ and $W_{V(-9.81)}$, $cm^3 \cdot cm^{-3}$) equilibrated on pressure ceramic plates. In both states of soil water saturation, air permeability (P_A) was also measured in the device designed to test the permeability of moulding sands (type LPiR-2e, Multiserw-Morek, Poland), to give the values

 VoR: https://doi.org/10.1016/j.still.2013.12.008

of $P_{A(-15.54)}$ and $P_{A(-9.81)}$. During the measurements pores with an equivalent diameter < 18.3 and < 29 μm, respectively, were filled with water, and larger pores were accessible for air. These measurements were carried out at the constant ambient temperature (20±0.5°C), therefore the dynamic viscosity of air did not require consideration. The results of the air permeability were given in 10^{-8} $m^2 \cdot Pa^{-1} \cdot s^{-1}$. In the additional 6 samples collected into the corresponding cylinders, saturated hydraulic conductivity (K_S, $m \cdot d^{-1}$) was measured using the Wit's apparatus (Eijkelkamp).

Total porosity of the soil (P_O, $cm^3 \cdot cm^{-3}$) was then calculated on the basis of the soil bulk and soil particle density. Thus, the relative volume of air-filled pores at both amounts of soil water was determined, hence defining the share of macropores with equivalent diameters greater than 18.3 μm ($V_{V(-15.54)} = P_O - W_{V(-15.54)}$; $cm^3 \cdot cm^{-3}$), as well as greater than 29 μm ($V_{V(-9.81)} = P_O - W_{V(-9.81)}$; $cm^3 \cdot cm^{-3}$).

2.2. Preliminary image analysis

From the above-mentioned layers of the pedon, samples with preserved structure were taken in the vertical plane into metal boxes measuring 8×9×4 cm. After being dried at room temperature, the soil was impregnated with a resin solution composed of polyester resin Polimal-109 (100.00 parts per volume), monostyrene (diluent, 60.00 parts per vol.), cyclohexanone hydroperoxide pasted in dibutyl phthalate (catalyst, 0.50 parts per vol.) and cobalt (III) naphthenate (activator, 0.15 parts per vol.). Impregnation was carried out in a vacuum desiccator, at a pressure of 27–33 hPa. Polymerization of the resin took about 6–10 weeks. The hardened blocks were then cut into 1-centimetre-thick slices. The obtained surfaces were subsequently levelled and polished with powder and corundum abrasive paper of different grain size from 80 to 1000 (Domżał and Słowińska-Jurkiewicz, 1987; Słowińska-Jurkiewicz et al., 2012). For each tested layer, eight 8×9 cm in size resin-impregnated opaque soil blocks were made. Afterwards, the soil opaque block faces were scanned using an Epson Perfection 1200 Photo scanner at a resolution of 1200×1200 dpi with 24-bit colour depth. Finally, each image was ca. 4000 by 4000 pixels. One of the eight series of the photographs of soil opaque blocks is presented in Fig. 1. On the basis of the soil blocks and their enlarged photos, morphological structure analysis of the tested chernozem was performed.

In the next step, the blue channel was isolated from the colour images (which was characterized by the best contrast), and relevant information was extracted for further analysis. The obtained images were recorded in 256 shades of grey, with prior improving of their contrast and intensity. The subsequent operations on the images were made using the

 VoR: https://doi.org/10.1016/j.still.2013.12.008

image analysis program Aphelion (Adcis SA). First, the images were thresholded, and a threshold level (the limit value of grey level between the solid phase and pores), was selected manually based on the brightness histogram and visual evaluation of an enlarged photo of the opaque block. In the obtained binary (B&W) images, the pores were marked with white, while the solid phase was marked with black colour. The white objects, i.e. cross-sections of pores, were then subjected to measurements. In addition to these images, images with an extra set of pores were prepared. For this purpose, by way of the image editing application Corel Photo-Paint, 1-bit images (B&W) were converted to 8-bit images (in greyscale). Next, spike noise with a density of 5% was added, which placed randomly spaced single white points on the images. Finally, the images were processed again into 1-bit. In this way, 8 binary images without noise and with noise were obtained for each layer, CHha1o–CHha5o and CHha1n–CHha5n, respectively. Then, the binary images were closed. This morphological operation was performed on 12 levels, i.e. with the square structuring element sized from 1 to 12. For each layer, 26 series of 8 images were obtained in this way: 1 series of images without noise, 1 series of images with noise, and also 12 series of images without noise after closing (c1–c12) and 12 – with noise after closing (c1–c12). For each image, the soil macroporosity was measured as the ratio of the area occupied by the cross-sections of the soil pores against the area of the entire image. Then, for each series of images, the average macroporosity was calculated. In this respect, under the laws of stereology (Russ and Dehoff, 2000), the relative area of the obtained macropores ($A_{A(im)}$) was equal to the relative volume of the macropores ($V_{V(im)}$, $cm^3 \cdot cm^{-3}$) in the analysed soil samples.

Due to the used scanning resolution, the value $V_{V(im)}$ corresponded to the relative volume of pores having an equivalent diameter greater than 21.2 μm. This is virtually equal to the field air capacity, which (depending on the level of the ground water table) is the share of air-filled macropores at a soil water potential in the range from –9.81 to –31 kPa. The macroporosity values obtained in this study by image analysis approximated most closely the macroporosity measured at the soil water potential of –15.54 kPa and –9.81 kPa, which correspond to shares of pores with equivalent diameters above 18.3 μm ($V_{V(-15.54)}$) and above 29 μm ($V_{V(-9.81)}$), respectively.

Concordance of the 26 average macroporosity values obtained by image analysis ($V_{V(im)}$) and the 2 laboratory measurements ($V_{V(-15.54)}$, $V_{V(-9.81)}$) was checked using the Student's or Satterwhite's t-test. The averages were deemed to be statistically not different when $P > 0.05$ (Table 1). This allowed for final selection of the images with macroporosity most similar to the macroporosity measured in the laboratory. Only these images were subject to further

 VoR: https://doi.org/10.1016/j.still.2013.12.008

analysis.

2.3. Extended image analysis

The performed preliminary calculations and statistical tests allowed to prepare 4 sets of images representing the analysed layers of the chernozem. Set 1 included images without noise and with the highest concordance of $V_{V(im)}$ and $V_{V(-9.81)}$: CHha1o, CHha2o, CHha3o, CHha4o-c5, and CHha5o-c6 (Fig. 2). Set 2 included images without noise and with the highest concordance of $V_{V(im)}$ and $V_{V(-15.54)}$: CHha1o, CHha2o, CHha3o-c2, CHha4o-c6, and CHha5o-c11 (Fig. 3). Bearing in mind the above-mentioned results of the statistical analysis (Table 1), one should notice that images CHha1o and CHha2o were used in sets 1 and 2. The duplicated images were characterized by a macroporosity most similar to both the macroporosity at –9.81 kPa and at –15.54 kPa.

Set 3 included images with noise and characterized by the highest concordance of $V_{V(im)}$ and $V_{V(-9.81)}$: CHha1n, CHha2n, CHha3n, CHha4n-c4, and CHha5n-c3 (Fig. 4). And finally, set 4 included images with noise and with the highest concordance of $V_{V(im)}$ and $V_{V(-15.54)}$: CHha1n, CHha2n, CHha3n-c1, CHha4n-c4, and CHha5n-c5 (Fig. 5). For the same reason as for sets 1 and 2, sets 3 and 4 include duplicate images CHha1n, CHha2n, and CHha4n-c4.

On the selected images (each in 8 replications), morphological operations and calculations were performed with use of the Aphelion software as described below.

Subsequent dilations were performed on each image, increasing the size of the square structuring element from k = 1 to n, from the relevant for each image initial macroporosity $V_{V(im)}$, to the achievement of $V_{V(im)n} = 1$. This allowed to calculate the index of soil pore network growth rate, v_G ($cm^3 \cdot cm^{-3}$), which reflected the degree of soil pore connectivity. The growth rate index was calculated as: $v_G = (1–V_{V(im)})/n$.

Then, the number of dilation steps (percolation number, n_{per}) was assessed at which all soil pores merge into a continuous network during the execution of the subsequent dilations, with the square structuring element sized from k = 1 to n. This phenomenon is accompanied by a change in the Euler's number sign (connectivity number, ε) for the binary image from positive to negative (Vogel, 1997; Vogel et al., 2010; Schlüter et al., 2011). The value of the percolation number n_{per} (Ghanbarian-Alavijeh and Hunt, 2012; Hunt and Ewing, 2009) was calculated for ε = 0. For this purpose, the lowest positive value ε_k and the highest negative value ε_{k+1} was found, and their corresponding values n_k and n_{k+1} were derived. Subsequently, by solving the set of two linear equations, the following was calculated: $n_{per} = n_k – \varepsilon_k \cdot [n_{k+1} – n_k)/(\varepsilon_{k+1} – \varepsilon_k)]$.

 VoR: https://doi.org/10.1016/j.still.2013.12.008

For each image, the value of the relative perimeter length of pore cross-sections L_A ($cm \cdot cm^{-2}$) was determined. This was used to calculate the average cross-sectional size of the pore (λ_P, mm): $\lambda_P = \pi (A_{A(im)}/L_A)$. The total length of pore path (L_P, cm) was also measured after the determination of the minimal skeleton of pore systems in the images.

The volumes of pores intersecting the 10-pixel-wide edge of the image were calculated. Such pores may be construed as coming into contact with the external environment, so water and air can be introduced through them into the soil sample. The relative volume of pores overlapping the left and right ($V_{V(L+R)}$), and the top and bottom edge ($V_{V(U+D)}$, $cm^3 \cdot cm^{-3}$) of the image was determined. Moreover, the relative volume of pores connecting the left and right ($V_{V(hor)}$) and the top and bottom edge of the image ($V_{V(vert)}$, $cm^3 \cdot cm^{-3}$) was measured. These were groups of pores responsible for the horizontal and vertical transport of fluids in the soil, respectively. The above-mentioned pores could be regarded as active during the flow of water and air through the soil.

The Pearson's linear correlation coefficients between the parameters' values obtained from image analysis for the 4 sets of images described above: $V_{V(im)}$, $V_{V(L+R)}$, $V_{V(U+D)}$, $V_{V(hor)}$, $V_{V(vert)}$, n_{per}, v_G, λ_P, and L_P, and the values of the parameters obtained from laboratory measurements: log K_S, log $P_{A(-9.81)}$, log $P_{A(-15.54)}$, $V_{V(-9.81)}$, and $V_{V(-15.54)}$ were calculated. Due to the large range of air and water permeability values, logarithmic data were used.

3. Results

3.1. Macrostructure

The macrostructure of the chernozem is presented in Fig. 1. Figs. 2–5 show the corresponding binary images of one of the eight series of soil opaque blocks for sets 1–4, respectively. The macrostructure was described using the terminology given by Aguilar et al. (2013) and Słowińska-Jurkiewicz et al. (2012). According to those authors, soil structure is related with the size, shape and arrangement of the primary particles and the voids in aggregate and non-aggregate materials, and the size, shape and arrangement of any aggregates present.

The discontinuous O horizon was mainly formed by loosely arranged hornbeam and oak leaves (Fig. 1, CHha1). In the soil under consideration, soil fauna activity was extensive and bioturbations were one of the most important processes shaping the whole pedon. The upper part of the A *mollic* horizon (CHha1) was characterized by very low compactness and bulk density of 0.86 $Mg \cdot m^{-3}$. In addition, horizons A (CHha1 and CHha2) and AC (CHha3 and CHha4) had an aggregate structure with crumbs (porous aggregates with more or less spheroidal shapes) developed to varying degrees. Biogenic channels and chambers were the

dominant pores. Tubular channels had generally smooth walls and varied in shape (circular, elliptical or elongated) according to the angle at which the cross-section was made. Chambers had spherical shapes and smooth walls. In the opaque blocks they were discernible as irregularly shaped non-connecting poroids (pore cross-sections), which were roughly equant and had smooth walls. In that part of the pedon, the soil bulk density was fairly equal (1.23–1.36 $Mg \cdot m^{-3}$), reaching 1.48 $Mg \cdot m^{-3}$ in the parent material horizon. The Ck horizon (CHha5) was loess of non-aggregate structure, with slight changes due to bioturbations, and pores in the form of vughs. In opaque blocks they were visible as non-connecting, irregular poroids which were roughly polygonal (mostly triangular or rectangular) with concave walls occurring between welded aggregates.

3.2. Water and air permeability

Selected chemical and physical properties of the studied chernozem are presented in Table 2. The mineral phase of the analysed chernozem had the texture of silt loam. The total organic carbon in the A horizon was 7.8–15.9, in the AC horizon 3.4–4.2, and 2.3 $mg \cdot g^{-1}$ in Ck. The soil was characterized by neutral and alkaline reaction, and carbonates were present in AC and Ck horizons below 75 cm, in an amount from 55 to 111 $mg \cdot g^{-1}$. The particle density of the soil gradually increased with the depth from 2.62 to 2.73 $Mg \cdot m^{-3}$.

The chernozem saturated hydraulic conductivity decreased along with increasing depth, with the most drastic decline observed between the layers 0–8 cm and 26–34 cm. In the three middle layers of the pedon, water conductivity increased slightly, undoubtedly due to the presence of some wide biogenic channels in this zone. In the deepest layer, it ultimately reached the value of only 0.05 $m \cdot d^{-1}$.

Air permeability at both studied potentials of soil water in the chernozem pedon showed a constant downward trend in the increasingly deeper layers and varied widely from about 5000 to $2.5 \cdot 10^{-8} \cdot m^2 \cdot Pa^{-1} \cdot s^{-1}$. Very high air permeability values were characteristic of both layers in the A *mollic* horizon.

Air capacity at both soil water potentials was characterized by a similar trend within the pedon, although, of course, the air capacity at –15.54 kPa was larger than the air capacity at –9.81 kPa. The highest air capacity revealed the 0–8 cm layer. The soil in the three middle layers of the pedon had air capacity by 1.5–2 times lower than the top layer, and the values progressively increased with depth. In the bottom layer (Ck horizon), further reduction of air capacity by about half was recorded.

 VoR: https://doi.org/10.1016/j.still.2013.12.008

3.3. Morphometric characteristics of soil pores

For the 4 sets of images (Table 3, Figs. 2–5), morphometric parameters were established that characterize the arrangement of soil pores. The correlation of the results of image analysis and laboratory permeability measurements was checked by calculating correlation coefficients (r). The values $|r| \geq 0.8783$ for $P < 0.05$, $|r| \geq 0.9587$ for $P < 0.01$, and $|r| \geq 0.9911$ for $P < 0.001$ were statistically significant.

Set 1 included images on which the noise was not applied. For these images, the highest similarity of $V_{V(im)}$ and $V_{V(-9.81)}$ values was assumed (Table 1 and 3). Hence, the images that corresponded to layers 90–98 and 120–128 cm were subjected to closing (5 and 6 steps, respectively). As a result, the values $V_{V(im)}$ and $V_{V(-9.81)}$ were very strongly correlated (Table 4). Similarly, the total length of pore path L_P was closely correlated with the value $V_{V(-9.81)}$, as the length of pores is strongly dependent on the relative area (and on the volume as well) of the pore system. However, the most interesting were the correlations between the parameters characterizing soil filtration abilities (log K_S and log P_A) and the parameters obtained from the image analysis. Saturated hydraulic conductivity turned out to be significantly correlated with macroporosity $V_{V(im)}$ (Fig. 6a) and with the relative volumes of pores contacting with left and right $V_{V(L+R)}$ and the bottom and top edge of the image $V_{V(U+D)}$ (Fig. 6b), and also with the relative volumes of pores extending through the whole sample horizontally $V_{V(hor)}$ and vertically $V_{V(vert)}$. Air permeability at the potential of –9.81 kPa (log $P_{A(-9.81)}$) was significantly correlated with the v_G parameter which reflects the degree of soil pore connectivity (Fig. 6c).

Set 2 included images on which the noise was not applied. For these images, the highest convergence of $V_{V(im)}$ and $V_{V(-15.54)}$ values was assumed (Table 1 and 3). Thus, the images representing layers 60–68, 90–98 and 120–128 cm underwent closing (2, 6, and 11 steps, respectively). Air capacities at the potential of –15.54 kPa are slightly larger than at the potential –9.81 kPa; therefore, a significant increase in the initial macroporosity of images, through a higher number of closing steps, was necessary. Similarly, as in the case of the 1. set of images, the values $V_{V(im)}$ and L_P were significantly correlated with $V_{V(-15.54)}$ (Table 4). Apart from this, the value K_S displayed a significant correlation with macroporosity $V_{V(im)}$ (Fig. 6d) and the relative volume of the pores being in contact with the left and the right edge of the image $V_{V(L+R)}$, and also with the relative volumes of pores extending through the whole sample horizontally $V_{V(hor)}$ and vertically $V_{V(vert)}$. Air permeability at the potential of –15.54 kPa (log $P_{A(-15.54)}$) was significantly correlated with the v_G parameter and also with the total length of pore path L_P (Figs. 6e and 6f).

 VoR: https://doi.org/10.1016/j.still.2013.12.008

Set 3 included images on which the noise was applied in order to model the small soil pores that, to a limited extent, were recorded when scanning the soil opaque blocks faces. For these images, the highest similarity of $V_{V(im)}$ and $V_{V(-9.81)}$ values was assumed (Table 1 and 3). The images representing layers 90–98 and 120–128 cm underwent closing (4 and 3 steps, respectively). As with the 1. and the 2. sets of images, the values $V_{V(im)}$ and L_P were significantly correlated with $V_{V(-9.81)}$ (Table 4). The K_S value showed significant correlation with macroporosity $V_{V(im)}$ (Fig. 6g) and the relative volume of the pores overlapping the left and the right $V_{V(L+R)}$ edge and the top and the bottom $V_{V(U+D)}$ edge of the image, as well as with relative volumes of pores extending through the whole sample vertically $V_{V(vert)}$. Furthermore, the water permeability was significantly negatively correlated with the value v_G (Fig. 6h), and significantly positively correlated with the average size of the pore cross-section λ_P (Fig. 6i). However, no statistically significant correlation between air permeability (log $P_{A(-9.81)}$) and the parameters obtained from image analysis was found.
Set 4 included images on which noise was applied. For these images, the highest convergence of $V_{V(im)}$ and $V_{V(-15.54)}$ values was assumed (Table 1 and 3). The images representing layers 60–68, 90–98 and 120–128 cm were subjected to closing (1, 4, and 5 steps, respectively). Similarly to the other sets of images, the values $V_{V(im)}$ and L_P were significantly correlated with $V_{V(-15.54)}$ (Table 4). The K_S value showed significant correlation to macroporosity $V_{V(im)}$ (Fig. 6j) and the relative volume of the pores being in contact with the left and the right $V_{V(L+R)}$ edge and the top and the bottom $V_{V(U+D)}$ edge of the image, as well as to relative volumes of pores extending through the entire sample vertically $V_{V(vert)}$. Moreover, water permeability was significantly negatively correlated with the value v_G (Fig. 6k), and significantly positively correlated with λ_P and L_P (Fig. 6l). However, no statistically significant correlation between air permeability (log $P_{A(-15.54)}$) and the parameters obtained from image analysis was found.

4. Discussion

Bryk et al. showed (2000), on the basis of structure standards, that the macroporosity obtained by image analysis is usually smaller than the field air capacity, although both parameters are strongly correlated with each other. The size of underestimation is closely related to the resolution used for the scanning or photographing of soil specimens (Carey et al., 2007). Increasing the resolution makes the image-analysis measured macroporosity more similar to macroporosity obtained from soil-water characteristic curve. This study showed that this effect is especially visible for high-porosity samples (Figs. 1–5, CHha1–CHha3). For

specimens with lower porosity (Figs. 1–5, CHha4 and CHha5), the relative volume of macropores by image analysis was about two times smaller than the respective field air capacity. When searching for the best representation of the actual soil pore system for the tested chernozem, we aimed at obtaining images with macroporosity that would be as close as possible to air capacity at potentials –15.54 and –9.81 kPa. Therefore all the images representing the 90–98 cm (CHha4) and 120–128 cm (CHha5) layers, and some images for the 60–68 cm (CHha3) layer were modified by applying the morphological closing, and, if necessary, having previously applied noise, which modelled tiny pores. In this way, four sets of images were prepared, for which morphometric indices were measured.

To assess the soil pore system, several morphometric parameters were selected. Their usefulness in the study proved to be diverse. In all the sets, statistically significant correlations between K_S and $V_{V(vert)}$ were found, and for the sets 1 and 2, also with $V_{V(hor)}$. Nevertheless, the measured values of these relative volumes (Table 3) often equalled 0. Hence, it is dubious whether these correlations are physically meaningful. Macropores in soil usually are not interconnected with themselves but are connected by smaller-sized pores or narrow ‘necks’ (Jarvis, 2007). Thus, macropores do not form a continuous system (Shaefer et al., 1997). This observation was confirmed through our study. In about 70–85% of the specimens (depending on the set), vertical or horizontal pores connecting the opposite edges of the sample were not found. In the remaining specimens, only one or two isolated pores of this type were detected. Consequently, corresponding values of $V_{V(vert)}$ and $V_{V(hor)}$ were minimal. The $V_{V(L+R)}$ and $V_{V(U+D)}$ parameters proved to be more useful as a good estimate of the volume of pores responsible for, respectively, the horizontal and vertical transport of water in the soil.

In forest soils, the activity of plant roots and soil mega- and mesofauna creates a variety of wide pores (Hayashi et al., 2006) that water may flow preferentially (Weiler and McDonnell, 2004). However, in the tested chernozem, the correlation between the average size of the pore cross-section λ_P and the water K_S and air P_A permeability was ambiguous. It appears that though the rate of water movement in soil will of course depend on the size of soil pores, still the continuity of soil pores and their ability to allow unobstructed flow of water remain the determining parameters. If a continuous pore path exists in the soil, increasing the pore diameter will obviously induce an increase in water permeability; however, large but isolated pores (e.g. chambers) will not be able to transport water at all. This is clearly visible in the images for layers of 26–34 cm (Figs. 1–3, CHha2) and 90–98 cm (CHha4) and in Table 3 – set 1 and 2.

It is noteworthy that strong positive correlations between v_G and P_A were observed for the 1.

 VoR: https://doi.org/10.1016/j.still.2013.12.008

and 2. sets of images (Table 4). Both parameters relate in fact to the same soil feature – pore connectivity. Higher values of the index of soil pore network growth rate v_G indicated a higher degree of connectivity of the soil pores. As regards air permeability, it is a sensitive measure of perviousness (and connectivity) of soil pores (Słowińska-Jurkiewicz, 1986). On the other hand, even though parameter n_{per} showed quite a strong correlation with filtering properties measured in laboratory, the correlation coefficients were not statistically significant. This parameter needs to be tested on a larger number of images of the soil structure.

As a consequence of the scanning resolution applied in the study, the value $V_{V(im)}$ represented the relative volume of pores with the equivalent diameter above 21.2 μm, which approximated air capacities at the soil water potential of –15.54 kPa and –9.81 kPa. The choice between $V_{V(-9.81)}$ and $V_{V(-15.54)}$ is debatable. Both values estimate $V_{V(im)}$ with sufficient accuracy. What's more, measurements of these air capacities, and also water capacities and air permeabilities at both soil water potentials, are routinely performed in soil physics laboratories, which provides a complete set of data characterizing water and air properties of the soil. These can be subsequently compared with the results of image analysis.

Images where noise was added in order to model the tiny soil pores lost during scanning, in view of our study, appeared to be less useful than the images which were not modified in this way. The noise induced equalisation of indices characterizing the soil pore connectivity (v_G, n_{per}) for the subsequent layers of chernozem. A suitable way of modifying images in order to equalize their macroporosity with the laboratory results is through performing the operation of closing with the number of steps individually selected for each image, depending on the initial difference in the macroporosities. Closing is a morphological operation which retains the basic character of the pore system in the analysed soil. When the size of the structuring element increases (Wojnar, 1999), a gradual connecting of neighbouring pores and a gentle rise of macroporosity occurs.

5. Conclusions

The macroporosity obtained by image analysis is usually smaller than the field air capacity derived from soil-water characteristic curve. Our study showed that this effect was especially visible for low-porosity samples. In order to overcome this phenomenon we modified the images of soil structure by morphological closing and, if necessary, having previously applied noise which modelled tiny pores lost during scanning. However, the images where noise was added, in view of our study, appeared to be less useful than the images which were not

modified in this way. The study indicated that the morphological operation of closing sufficed to successfully equalize the macroporosity derived from image analysis with the laboratory results.

Selected morphometric indices were measured on the prepared images of the chernozem structure and subsequently their usefulness was tested. The relative volumes of pores contacting with left and right and the bottom and top edges of the image proved to be a good estimate of the volume of pores responsible for, respectively, the horizontal and vertical transport of water in the soil. The index of soil pore network growth rate represented quite reasonably the air permeability.

Our study demonstrated that water and air permeability and the air capacity in the chernozem decreased with the depth. Along with the laboratory-measured saturated hydraulic conductivity, the image-analysis derived macroporosity and the relative volumes of pores overlapping the left and right and the bottom and top edge of the image decreased. Air permeability was positively correlated with the index of soil pore network growth rate. In our study, the morphological and morphometric image analysis confirmed that the most important parameters controlling the transportation of fluids in the soil is the connectivity of pores, as well as their volume. On the basis of the results obtained from the image analysis (e.g. $V_{V(L+R)}$, $V_{V(U+D)}$, v_G, L_P), qualitative conclusions can be made regarding the level of water and air permeability of the analysed soil.

Acknowledgements

The part of the research regarding the soil structure was financed from the budget for science in Poland in 2010–2013, grant no. N N310 447938. The remaining results presented in the article were obtained within the scope of the statutory research conducted at the University of Life Sciences in Lublin (Institute of Soil Science, Environment Engineering and Management) and financed from the budget of the Ministry of Science and Higher Education in Poland.

References

Aguilar, J., Dorronsoro-Fdez, C., Fernández, J., Dorronsoro Diaz, C., Martin, F., Dorronsoro, B., 2013. Soil Microscopy. Soil Micromorphography. Interactive multimedia programme for self-studying soil thin section description. http://edafologia.ugr.es/micgraf/indexw.htm (accessed on April 8, 2013).

Badorreck, A., Gerke, H.H., Hüttl, R.F., 2013. Morphology of physical soil crusts and

infiltration patterns in an artificial catchment. Soil & Tillage Research 129, 1–8.

Boizard, H., Yoon, S.W., Leonard, J., Lheureux, S., Cousin, I., Roger-Estrade, J., Richard, G., 2013. Using a morphological approach to evaluate the effect of traffic and weather conditions on the structure of a loamy soil in reduced tillage. Soil & Tillage Research 127, 34–44.

Bryk, M., 2009. Hydraulic conductivity and index of soil physical quality of a forest Haplic Arenosol. Annales UMCS sec. E, Agricultura 64(4), 9–18.

Bryk, M., Domżał, H., Prangal, J., Słowińska-Jurkiewicz, A., 2000. An attempt to characterise soil macroporosity on the basis of structure standards. Acta Agrophysica 35, 23–30.

Bryk, M., Kołodziej, B., 2009. Reclamation problems for the area of a former borehole sulphur mine with particular reference to soil air properties. Land Degradation & Development 20, 509–521.

Bryk, M., Kołodziej, B., Serzysko, T., 2007. Effect of freezing on air properties of compacted Mollic Leptosol. Acta Agrophysica 9(3), 571–582.

Carey, S.K., Quinton, W.L., Goeller, N.T., 2007. Field and laboratory estimates of pore size properties and hydraulic characteristics for subarctic organic soils. Hydrological Processes 21, 2560–2571.

Domżał, H., Słowińska-Jurkiewicz, A., 1987. Effect of tillage and weather conditions on structure and physical properties of soil and yield of winter wheat. Soil & Tillage Research, 10, 225–241.

Ghanbarian-Alavijeh, B., Hunt, A.G., 2012. Unsaturated hydraulic conductivity in porous media: Percolation theory. Geoderma 187–188, 77–84.

Hayashi, Y., Ken'ichirou, K., Mizuyama, T., 2006. Changes in pore size distribution and hydraulic properties of forest soil resulting from structural development. Journal of Hydrology 331, 85–102.

Horn, R., Smucker, A., 2005. Structure formation and its consequences for gas and water transport in unsaturated arable and forest soils. Soil & Tillage Research 82, 5–14.

Hunt, A., Ewing, R., 2009. Percolation theory for flow in porous media. Lecture Notes in Physics 771, Springer, Berlin Heidelberg.

Jarvis, N.J., 2007. A review of non-equilibrium water flow and solute transport in soil macropores: principles, controlling factors and consequences for water quality. European Journal of Soil Science 58, 523–546.

Kołodziej, B., Bryk, M., Serzysko, T., 2007. Effect of freezing on air properties of compacted

lessivé soil. Soil Science Annual 58(3/4), 95–101.

Kutílek, M., 2004. Soil hydraulic properties as related to soil structure. Soil & Tillage Research 79, 175–184.

Kutílek, M., Nielsen, D.R., 2007. Interdisciplinarity of hydropedology. Geoderma 138, 252–260.

Mangalassery, S., Sjögersten, S., Sparkes, D.L., Sturrock, C. J., Mooney, S.J., 2013. The effect of soil aggregate size on pore structure and its consequence on emission of greenhouse gases. Soil & Tillage Research 132, 39–46.

Maruszewski, Z., Dembski, B., 2008. Application of numerical model for assessment of vertical drainage system efficiency for limitation of pollutants migration in ground waters. Annual Set The Environment Protection 10, 679–696.

PN-ISO 10390, 1997. Soil quality – Determination of pH. Polish Committee for Standardization, Warsaw, Poland.

PN-ISO 10693, 2002. Soil quality – Determination of carbonate content – Volumetric method. Polish Committee for Standardization, Warsaw, Poland.

PN-ISO 11508, 2001. Soil quality – Determination of particle density. Polish Committee for Standardization, Warsaw, Poland.

PN-ISO 14235, 2003. Soil quality – Determination of organic carbon by wet oxidation with dichromate (VI) in sulphuric (VI) acid. Polish Committee for Standardization, Warsaw, Poland.

Polish Society of Soil Science, 2009. Particle Size Distribution and textural classes of soils and mineral materials – Classification of Polish Society of Soil Science 2008. Soil Science Annual 60(2), 5–16.

Russ, J.C., Dehoff, R.T., 2000. Practical Stereology, second ed. Kluwer Academic/Plenum Publishers, New York, NY.

Schjønning, P., Thomsen, I.K., 2013. Shallow tillage effects on soil properties for temperate-region hard-setting soils. Soil & Tillage Research 132, 12–20.

Schlüter, S., Weller, U., Vogel, H.-J., 2011. Soil-structure development including seasonal dynamics in a long-term fertilization experiment. Journal of Plant Nutrition and Soil Science 174, 395–403.

Shaefer, C.E., Arands, R.R., van der Sloot, H.H., Kosson, D.S., 1997. Modeling of the gaseous diffusion coefficient through unsaturated soil system. Journal of Contaminant Hydrology 29, 1–21.

Słowińska-Jurkiewicz, A., 1986. Air permeability in forest and arable loess soils. Advances of

Agricultural Sciences – Problem Issues 315, 189–204.

Słowińska-Jurkiewicz, A., Bryk, M., Kołodziej, B., Jaroszuk-Sierocińska, M., 2012. Macrostructure of soils in Poland. AWR Magic, Lublin, Poland.

Słowińska-Jurkiewicz, A., Pranagal, J., Zawiślak-Pranagal, M., Bryk, M., 2001. Changes in soil filtering capabilities of an experimental field assigned for irrigation with wastewater. Advances of Agricultural Sciences – Problem Issues 475, 61–71.

Vogel, H.-J., 1997. Morphological determination of pore connectivity as a function of pore size using serial sections. European Journal of Soil Science 48, 365–377.

Vogel, H.-J., Cousin, I., Ippisch, O., Bastian, P., 2006. The dominant role of structure for solute transport in soil: experimental evidence and modelling of structure and transport in a field experiment. Hydrology and Earth System Sciences 10, 495–506.

Vogel, H.-J., Weller, V., Schlüter, S., 2010. Quantification of soil structure based on Minkowski functions. Computers & Geosciences 36, 1236–1245.

Weiler, M., McDonnell, J.J., 2004. Water storage and movement, in: Burley, J., Evans, J., Youngquist, J.A. (Eds.), Encyclopedia of Forest Sciences. Elsevier, Oxford, pp. 1253–1260.

Wojnar, L., 1999. Image analysis. Applications in materials engineering, CRC Press, Boca Raton, FL, USA.

VoR: https://doi.org/10.1016/j.still.2013.12.008

Table 1. Results of the statistical t-test after the preliminary image analysis; the same letters (a, b, A, B) for each sample denote statistically not different data at P = 0.05; A, B – the most similar data

Sample	$V_{V(-9.81)}$ ($cm^3 \cdot cm^{-3}$)	$V_{V(-15.54)}$ ($cm^3 \cdot cm^{-3}$)	$V_{V(im)}$ ($cm^3 \cdot cm^{-3}$)												
			(c0)[a]	-c1[b]	-c2	-c3	-c4	-c5	-c6	-c7	-c8	-c9	-c10	-c11	-c12
images without noise															
CHha1o	0.284 a A	0.298 b B	0.300 A B	0.305 a b	0.317 a b	0.332 a b	0.350 b								
CHha2o	0.132 a A	0.148 b B	0.149 A B	0.152 a b	0.159 b	0.167 b									
CHha3o	0.149 a A	0.166 b B	0.156 A b	0.160 a b	0.170 a B	0.184 a b	0.203 b								
CHha4o	0.153 a A	0.182 b B					0.131 a	0.154 A b	0.180 a B	0.206 b					
CHha5o	0.058 a A	0.083 b B	0.041 a b	0.042 a b	0.045 a b	0.048 a b	0.051 a b	0.055 a b	0.058 A b	0.063 a b	0.067 a b	0.072 a b	0.077 a b	0.082 a B	0.088 a b
images with noise															
CHha1n	0.284 a A	0.298 b B	0.303 A B	0.309 a b	0.325 a b	0.348 b									
CHha2n	0.132 a A	0.148 b B	0.153 A B	0.157 b	0.166 b										
CHha3n	0.149 a A	0.166 b B	0.160 A b	0.165 a B	0.179 a b	0.202 b									
CHha4n	0.153 a A	0.182 b B				0.127 a	0.160 A B	0.204 b							
CHha5n	0.058 a A	0.083 b B	0.045 a b	0.047 a	0.051 a	0.057 A	0.066 a	0.080 a B	0.104 b						

[a](c0) – unmodified images; [b]-c1, -c2, ... – the number of steps of the morphological closing

VoR: https://doi.org/10.1016/j.still.2013.12.008

Table 2. Selected chemical and physical properties of the Haplic Chernozem

Sample	Layer	Fractions ($g \cdot g^{-1}$)			ρ_s	ρ	pH		TOC	$CaCO_3$	K_S	log K_S	$P_{A(-9.81)}$	$P_{A(-15.54)}$	log $P_{A(-9.81)}$	log $P_{A(-15.54)}$	$V_{V(-9.81)}$	$V_{V(-15.54)}$
	(cm)	sand	silt	clay	($Mg \cdot m^{-3}$)	($Mg \cdot m^{-3}$)	H_2O	$CaCl_2$	($mg \cdot g^{-1}$)	($mg \cdot g^{-1}$)	($m \cdot d^{-1}$)		($10^{-8} \cdot m^2 \cdot Pa^{-1} \cdot s^{-1}$)				($cm^3 \cdot cm^{-3}$)	
CHha1	0–8	0.14	0.71	0.15	2.62	0.86	6.41	6.10	15.9	0	59.00	1.77	5140.5	5167.2	3.71	3.71	0.284	0.298
CHha2	26–34	0.13	0.65	0.22	2.66	1.37	7.00	6.30	7.8	0	0.21	–0.68	1820.8	1841.2	3.26	3.27	0.132	0.148
CHha3	60–68	0.19	0.59	0.22	2.67	1.36	7.62	7.00	3.4	55	0.28	–0.55	33.2	40.6	1.52	1.61	0.149	0.166
CHha4	90–98	0.09	0.74	0.17	2.70	1.23	8.46	7.66	4.2	111	1.54	0.19	7.5	23.5	0.88	1.37	0.153	0.182
CHha5	120–128	0.12	0.74	0.14	2.73	1.48	8.38	7.62	2.3	104	0.05	–1.30	2.4	2.4	0.38	0.38	0.058	0.083

 VoR: https://doi.org/10.1016/j.still.2013.12.008

Table 3. Results of the morphometric image analysis

	$V_{V(im)}$ ($cm^3 \cdot cm^{-3}$)	$V_{V(L+R)}$ ($cm^3 \cdot cm^{-3}$)	$V_{V(U+D)}$ ($cm^3 \cdot cm^{-3}$)	$V_{V(hor)}$ ($cm^3 \cdot cm^{-3}$)	$V_{V(vert)}$ ($cm^3 \cdot cm^{-3}$)	n_{per}	v_G ($cm^3 \cdot cm^{-3}$)	λ_P (mm)	L_P (cm)
Set 1									
CHha1o	0.300	0.270	0.129	0.090	0.159	5.1	0.012	0.417	898.0
CHha2o	0.150	0.015	0.036	0.000	0.000	8.0	0.013	0.259	544.6
CHha3o	0.156	0.015	0.024	0.000	0.000	5.6	0.011	0.199	628.4
CHha4o-c5	0.154	0.043	0.057	0.000	0.000	6.7	0.007	0.316	576.3
CHha5o-c6	0.059	0.023	0.029	0.000	0.000	28.6	0.005	0.355	127.8
Set 2									
CHha1o	0.300	0.270	0.129	0.090	0.159	5.1	0.012	0.417	898.0
CHha2o	0.150	0.015	0.036	0.000	0.000	8.0	0.013	0.259	544.6
CHha3o-c2	0.170	0.019	0.036	0.002	0.000	5.6	0.011	0.244	503.9
CHha4o-c6	0.180	0.023	0.125	0.044	0.000	6.9	0.006	0.390	427.2
CHha5o-c11	0.082	0.012	0.069	0.022	0.000	28.5	0.005	0.514	125.9
Set 3									
CHha1n	0.303	0.272	0.131	0.090	0.159	4.1	0.028	0.402	993.4
CHha2n	0.153	0.015	0.036	0.000	0.000	5.0	0.032	0.242	665.7
CHha3n	0.160	0.015	0.024	0.000	0.000	4.4	0.032	0.190	736.2
CHha4n-c4	0.160	0.036	0.044	0.000	0.000	5.0	0.030	0.244	642.6
CHha5n-c3	0.057	0.005	0.039	0.013	0.000	6.3	0.032	0.208	315.6
Set 4									
CHha1n	0.303	0.272	0.131	0.090	0.159	4.1	0.028	0.402	993.4
CHha2n	0.153	0.015	0.036	0.000	0.000	5.0	0.032	0.242	665.7
CHha3n-c1	0.165	0.014	0.029	0.002	0.000	4.4	0.032	0.208	649.1
CHha4n-c4	0.160	0.036	0.044	0.000	0.000	5.0	0.030	0.244	642.6
CHha5n-c5	0.080	0.013	0.048	0.014	0.000	6.3	0.032	0.219	391.3

 VoR: https://doi.org/10.1016/j.still.2013.12.008

Table 4. Correlation coefficients of the results of image analysis and laboratory measurements

	$V_{V(im)}$ ($cm^3 \cdot cm^{-3}$)	$V_{V(L+R)}$ ($cm^3 \cdot cm^{-3}$)	$V_{V(U+D)}$ ($cm^3 \cdot cm^{-3}$)	$V_{V(hor)}$ ($cm^3 \cdot cm^{-3}$)	$V_{V(vert)}$ ($cm^3 \cdot cm^{-3}$)	n_{per}	v_G ($cm^3 \cdot cm^{-3}$)	λ_P (mm)	L_P (cm)
Set 1									
log K_S	0.955*	0.920*	0.956*	0.894*	0.894*	–0.619	0.434	0.572	0.869
log $P_{A(-9.81)}$	0.786	0.624	0.620	0.671	0.671	–0.594	0.885*	0.187	0.742
$V_{V(-9.81)}$	0.997***	0.887*	0.898*	0.884*	0.884*	–0.720	0.630	0.411	0.946*
Set 2									
log K_S	0.977**	0.910*	0.753	0.891*	0.894*	–0.619	0.437	0.077	0.878
log $P_{A(-15.54)}$	0.756	0.665	0.141	0.390	0.664	–0.679	0.880*	–0.405	0.906*
$V_{V(-15.54)}$	1.000***	0.893*	0.621	0.799	0.876	–0.719	0.583	–0.092	0.944*
Set 3									
log K_S	0.955*	0.933*	0.896*	0.832	0.894*	–0.747	–0.971*	0.921*	0.870
log $P_{A(-9.81)}$	0.784	0.665	0.629	0.598	0.671	–0.678	–0.543	0.721	0.787
$V_{V(-9.81)}$	0.997***	0.913*	0.850	0.806	0.884*	–0.865	–0.890*	0.884*	0.958*
Set 4									
log K_S	0.960**	0.923*	0.866	0.831	0.894*	–0.747	–0.939*	0.922*	0.934*
log $P_{A(-15.54)}$	0.802	0.655	0.584	0.576	0.664	–0.726	–0.512	0.722	0.864
$V_{V(-15.54)}$	0.991**	0.897*	0.817	0.800	0.876	–0.853	–0.860	0.891*	0.978**

*P < 0.05, **P < 0.01, ***P < 0.001

 VoR: https://doi.org/10.1016/j.still.2013.12.008

Figure captions

Fig. 1. Structure of the studied Haplic Chernozem – (a) CHha1, 0–8 cm layer; (b) CHha2, 26–34 cm layer; (c) CHha3, 60–68 cm layer; (d) CHha4, 90–98 cm layer; (e) CHha5, 120–128 cm layer. Representative photographs in the 1:2 scale

Fig. 2. Set 1 of images without noise and with the highest concordance of $V_{V(im)}$ and $V_{V(-9.81)}$: (a) CHha1o; (b) CHha2o; (c) CHha3o; (d) CHha4o-c5; (e) CHha5o-c6. Representative binary images in the 1:2 scale; white colour indicates the solid phase and black – pores

Fig. 3. Set 2 of images without noise and with the highest concordance of $V_{V(im)}$ and $V_{V(-15.54)}$: (a) CHha1o; (b) CHha2o; (c) CHha3o-c2; (d) CHha4o-c6; (e) CHha5o-c11. Representative binary images in the 1:2 scale; white colour indicates the solid phase and black – pores

Fig. 4. Set 3 of images with noise and with the highest concordance of $V_{V(im)}$ and $V_{V(-9.81)}$: (a) CHha1n; (b) CHha2n; (c) CHha3n; (d) CHha4n-c4; (e) CHha5n-c3. Representative binary images in the 1:2 scale; white colour indicates the solid phase and black – pores

Fig. 5. Set 4 of images with noise and with the highest concordance of $V_{V(im)}$ and $V_{V(-15.54)}$: (a) CHha1n; (b) CHha2n; (c) CHha3n-c1; (d) CHha4n-c4; (e) CHha5n-c5. Representative binary images in the 1:2 scale; white colour indicates the solid phase and black – pores

Fig. 6. Selected correlation diagrams. Diagrams (a)–(c) – set 1; diagrams (d)–(f) – set 2; diagrams (g)–(i) – set 3; diagrams (j)–(l) – set 4. Thin line – 95% confidence band

Fig. 1

(a)

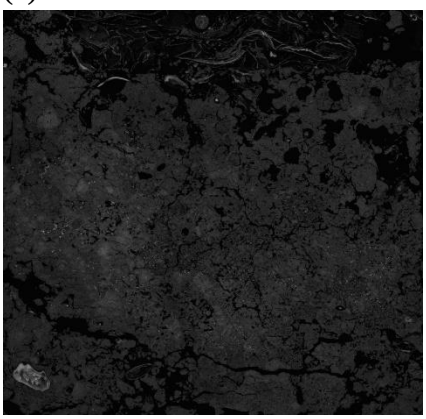

(b)

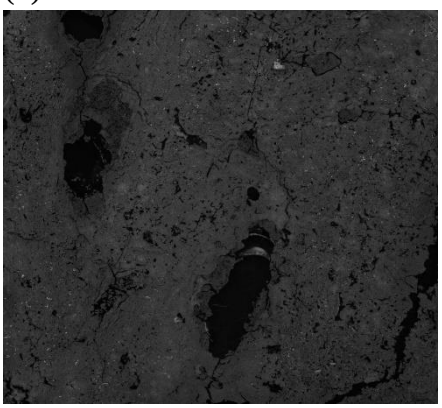

(c)

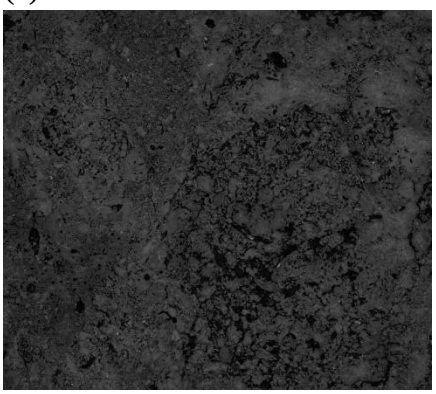

(d)

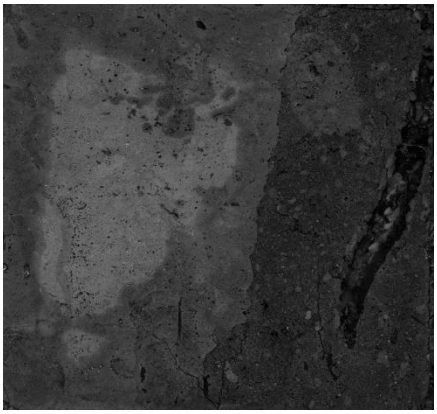

(e)

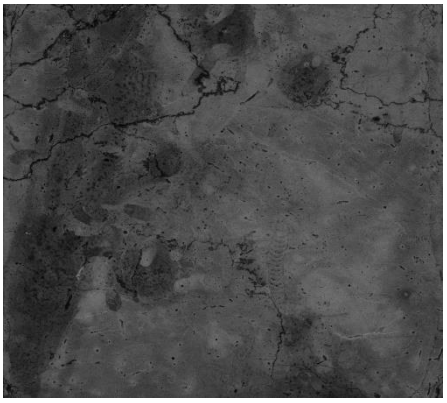

(a)

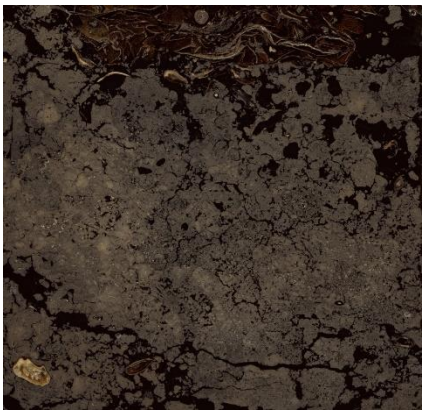

(b)

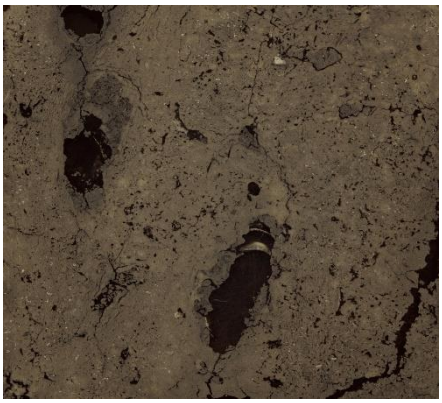

(c)

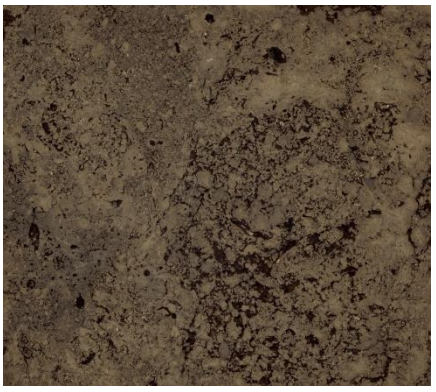

(d)

(e)

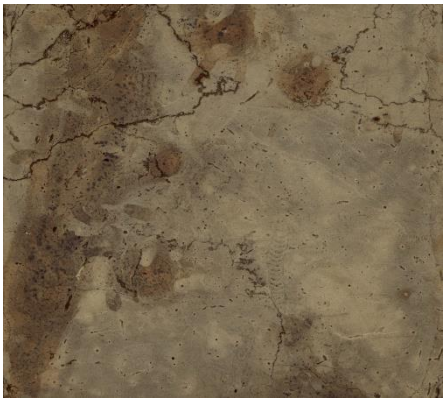

Fig. 2

(a)

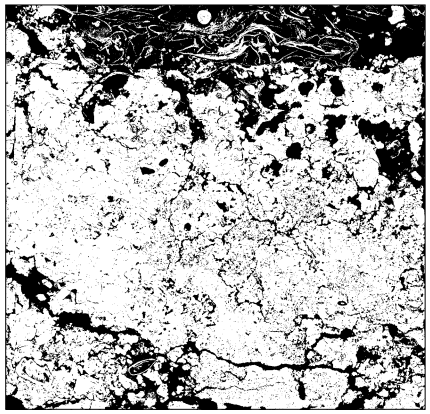

(b)

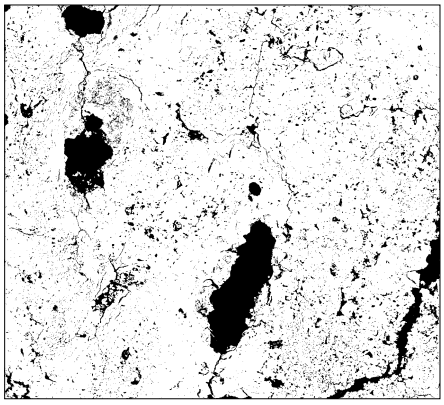

(c)

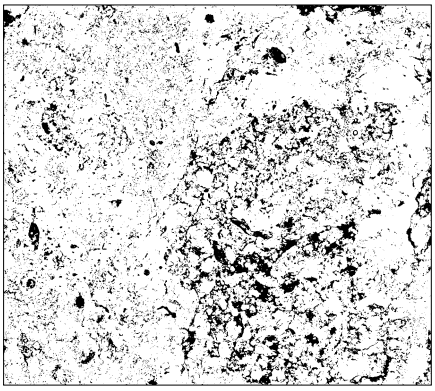

(d)

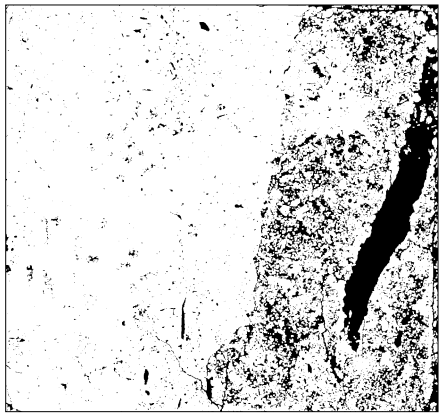

(e)

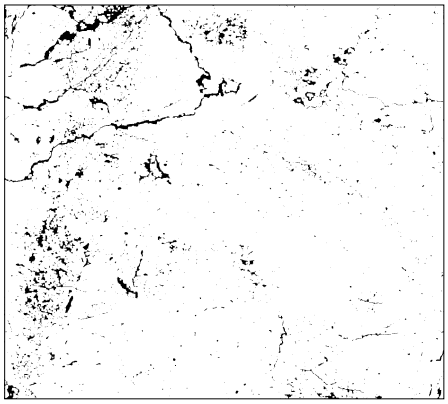

Fig. 3

(a)

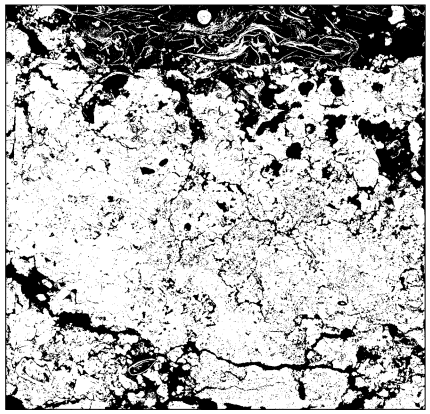

(b)

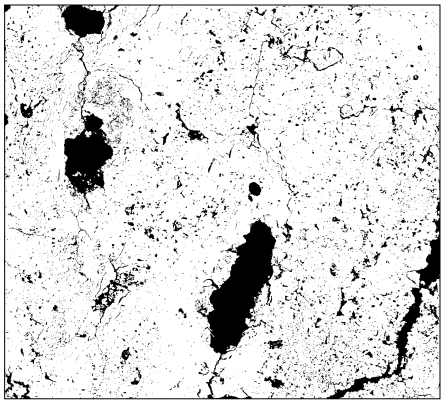

(c)

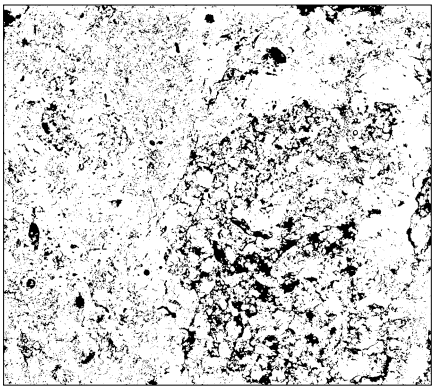

(d)

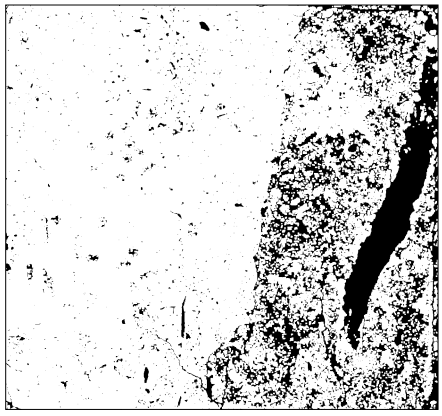

(e)

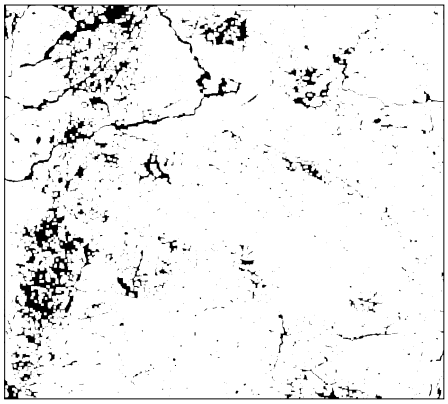

Fig. 4

(a)

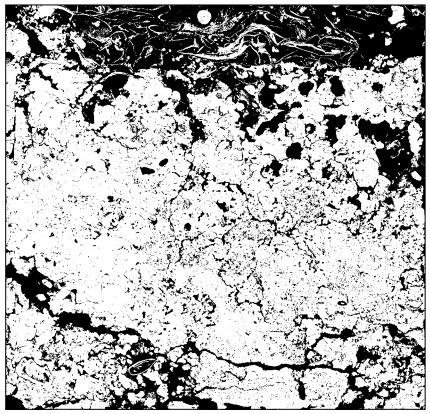

(b)

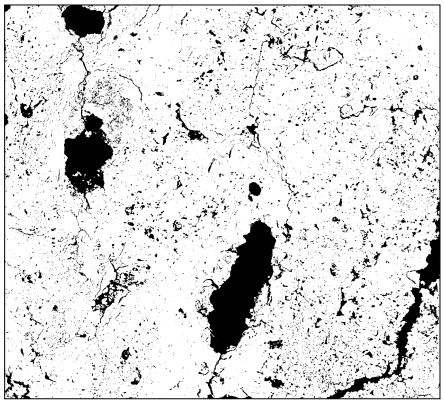

(c)

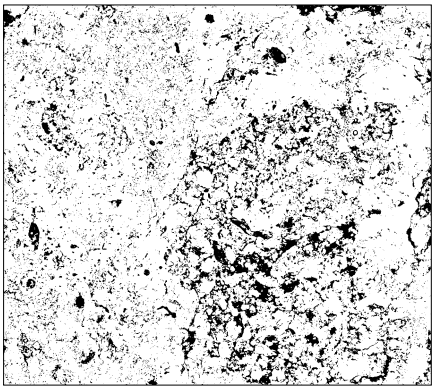

(d)

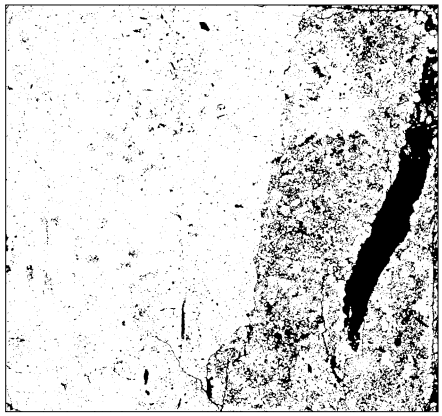

(e)

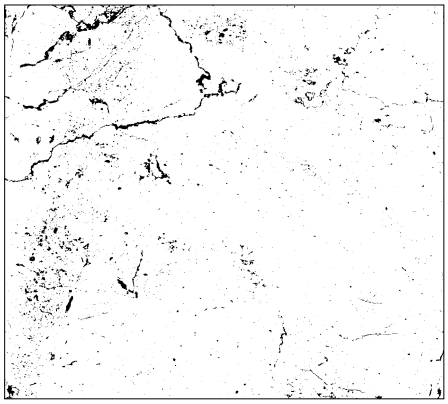

Fig. 5

(a)

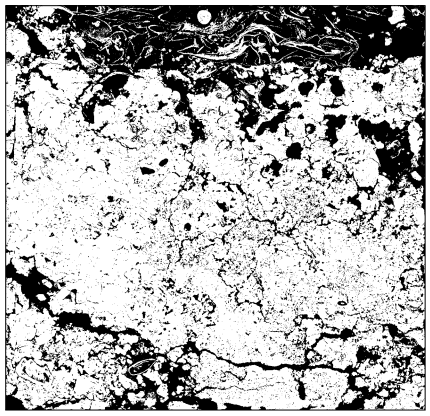

(b)

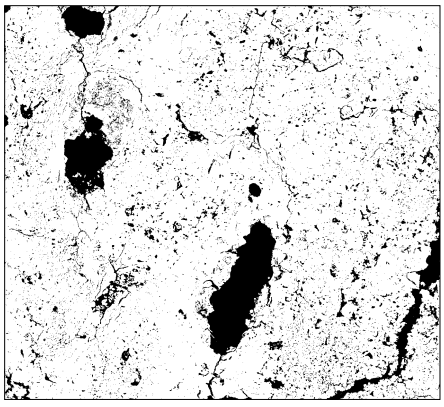

(c)

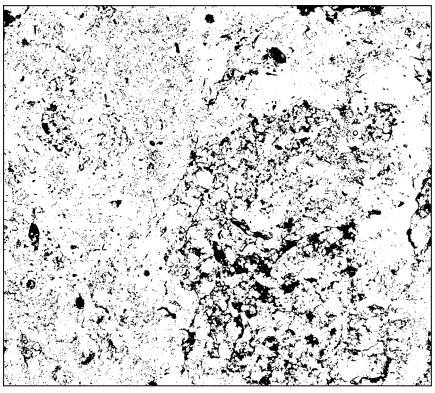

(d)

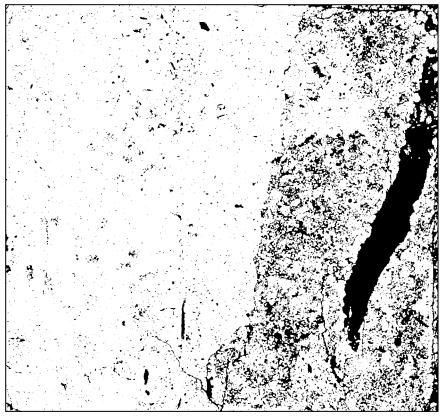

(e)

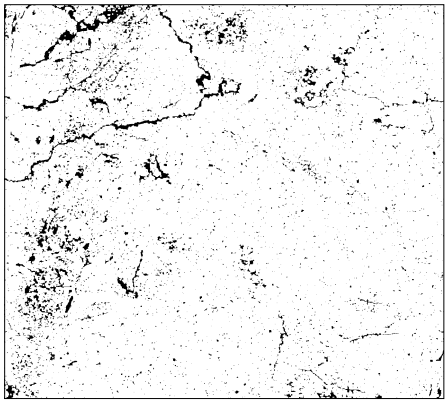

Fig. 6

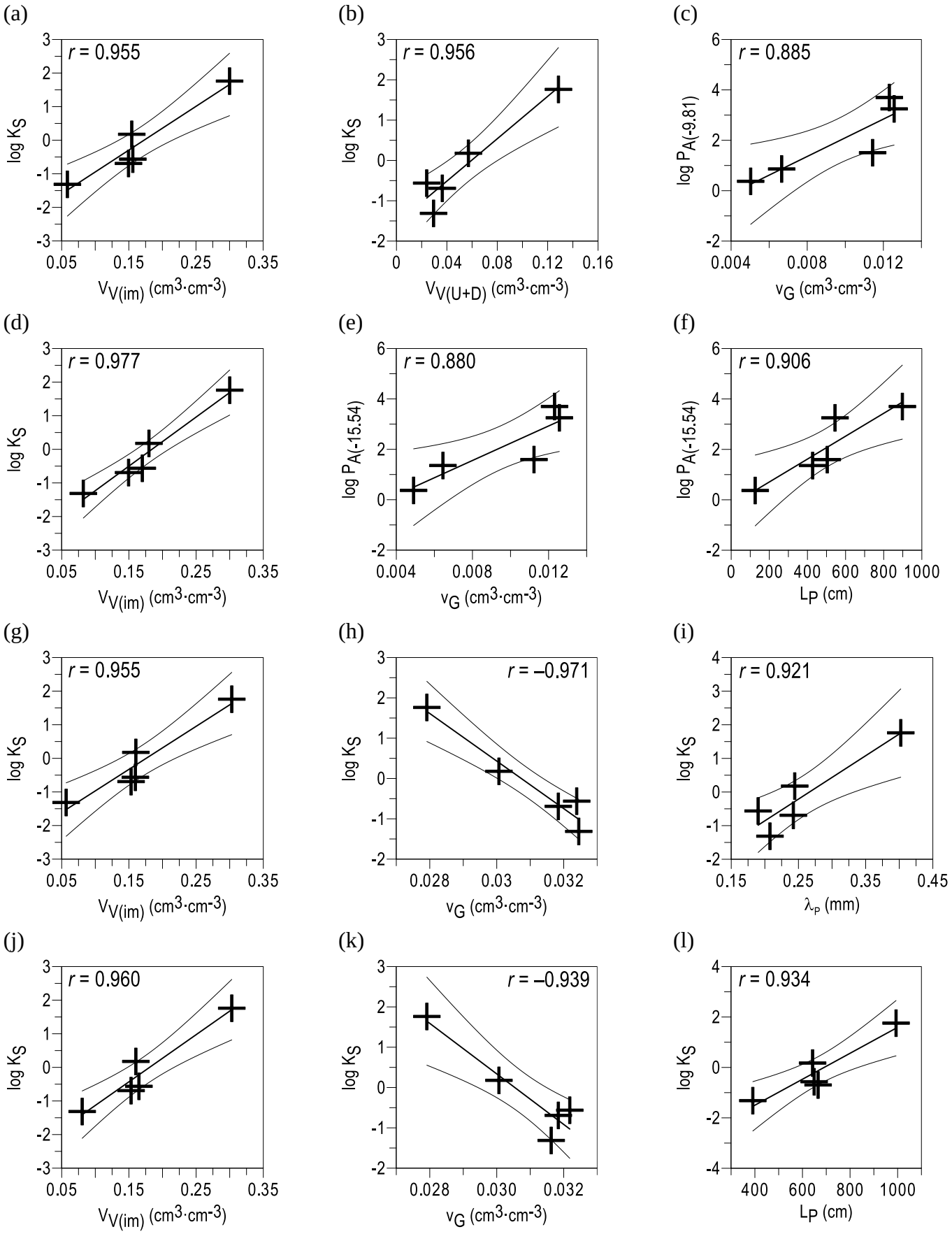
(a)
r = 0.955
log KS
VV(im) (cm3·cm-3)
(b)
r = 0.956
log KS
VV(U+D) (cm3·cm-3)
(c)
r = 0.885
log PA(-9.81)
vG (cm3·cm-3)
(d)
r = 0.977
log KS
VV(im) (cm3·cm-3)
(e)
r = 0.880
log PA(-15.54)
vG (cm3·cm-3)
(f)
r = 0.906
log PA(-15.54)
LP (cm)
(g)
r = 0.955
log KS
VV(im) (cm3·cm-3)
(h)
r = –0.971
log KS
vG (cm3·cm-3)
(i)
r = 0.921
log KS
λP (mm)
(j)
r = 0.960
log KS
VV(im) (cm3·cm-3)
(k)
r = –0.939
log KS
vG (cm3·cm-3)
(l)
r = 0.934
log KS
LP (cm)